Improved Gamma-Ray Point Source Quantification in Three Dimensions by Modeling Attenuation in the Scene

M. S. Bandstra, D. Hellfeld, J. R. Vavrek, B. J. Quiter, K. Meehan, P. J. Barton, J. W. Cates, A. Moran, V. Negut, R. Pavlovsky, and T. H. Y. Joshi

Abstract—**Using a series of detector measurements taken at different locations to localize a source of radiation is a well-studied problem. The source of radiation is sometimes constrained to a single point-like source, in which case the location of the point source can be found using techniques such as maximum likelihood. Recent advancements have shown the ability to locate point sources in 2D and even 3D, but few have studied the effect of intervening material on the problem. In this work we examine gamma-ray data taken from a freely moving system and develop voxelized 3-D models of the scene using data from the onboard LiDAR. Ray casting is used to compute the distance each gamma ray travels through the scene material, which is then used to calculate attenuation assuming a single attenuation coefficient for solids within the geometry. Parameter estimation using maximum likelihood is performed to simultaneously find the attenuation coefficient, source activity, and source position that best match the data. Using a simulation, we validate the ability of this method to reconstruct the true location and activity of a source, along with the true attenuation coefficient of the structure it is inside, and then we apply the method to measured data with sources and find good agreement.**

I. Introduction

SEARCHING for, localizing, and quantifying radioactive material using radiation detectors is a problem with a wide variety of applications, from finding lost sources, to mapping radioactive contamination after a nuclear accident, to stopping the transport of material at a border crossing [1], [2]. In many applications, the presence of passive material between the sources and the instrument, if not properly accounted for, can limit the ability of an operator to quantify the source and, e.g., lead to an underestimation or erroneous localization of the radioactivity. Often in these situations the attenuating material has three-dimensional structure, which adds another degree of complexity. Because of the difficulty in sensing and quantifying the attenuation and scattering by passive material, these effects are seldom accounted for in search applications, but nevertheless they can be of vital importance.

Many nuclear security, safety and non-proliferation applications using radiation detection and/or imaging systems can benefit from increased abilities to quantify sources in three-dimensional environments with attenuation from material in those environments. For example, better mapping of radioactive sources in three-dimensional volumes can help account for material stored in casks or waste drums in nuclear safeguards applications. In the event of a nuclear accident, the ability to rapidly map and quantify contamination, especially in complex areas like urban environments where the shielding from structures is important, could provide responders and the public with high-quality, actionable information needed to reduce their dose.

In some gamma-ray imaging applications where the quantification of radiological material is critical, techniques have been developed to simultaneously solve for the radiation source distribution and attenuation by passive material. Examples are in Positron Emission Tomography (PET) and Single Photon Emission Computed Tomography (SPECT) imaging, where algorithms have been developed to simultaneously image the target while optimizing the unknown attenuation due to material in the body [3], [4], [5]. Such techniques have been found to improve upon earlier techniques that used X-ray computed tomography (CT) to estimate the attenuation map [6]. For a recent review of this field, see [7]. Similar techniques have been developed for Passive Gamma Emission Tomography (PGET), where tomographic measurements are used to inspect spent nuclear fuel assemblies [8]. The optimizations required are nonconvex [7], so these techniques generally leverage the constrained detector-image geometry, a dense image space with a limited spatial extent that the detectors encircle, and predictable attenuation coefficients (e.g., human tissue or fuel pins). Generally these constraints are included in the form of regularization functions that are added to the loss function. Some techniques even incorporate non-attenuation contextual data such as magnetic resonance imaging (MRI) to aid in the reconstruction [9].

However, in the case of a freely moving detector system, none of these advantages remain. No longer is the space constrained, nor can one assume much if anything about the density of material in the scene, or even if the source is in the same plane as the detectors. Nevertheless, many have studied the problem of using a series of detector measurements to locate and measure the strength of a radiation point source, using a variety of different techniques, including maximum likelihood estimation [10], [11], [12], [13], [14], [15], Bayesian estimation [10], [16], [17], [18], [19], geometric

techniques [20], [21], particle filters [22], and clustering techniques [23]. Solutions to this problem have been demonstrated in 2D [10], [11], [16], [13], [14], [24], [25], and often a grid is used to simplify the calculations involved and to fully explore the nonconvex space [16], [17], [26]. Because of the computational complexity and the difficulty of obtaining a representative model of the measurement geometry and incorporating it into an algorithm, attenuation by intervening material is seldom considered [24], [25], [18], [19]. Only recently have source localization methods been applied in 3D without attenuation [27], [28]. In one recent work, 2-D point source localization was performed with precomputed attenuation coefficients to account for objects in the scene [18], and in another recent work 3-D point source localization was performed with unknown attenuation between the source and detector but the thicknesses and orientations of the attenuating objects were known [19]. Our recent work has demonstrated accurate quantitative reconstruction in 3D with freely moving systems in cases when attenuation can be ignored [15], [29], [30]. To our knowledge, the method has not been applied both in 3D and with attenuation by unknown objects.

As challenging as the SPECT and PGET reconstruction problems are, the problem of source reconstruction in 3D with a freely moving system has even fewer constraints, even before the simultaneous reconstruction of attenuation is considered. To make the problem tractable, we make four simplifying assumptions herein: (1) that we are searching for a single point source, (2) that the background is relatively constant, (3) that the contextual data from the LiDAR point cloud constrains where solid material in the scene can be, and (4) that all solid materials have the same attenuation coefficient. The objective of this work is to develop a method to solve this special case and to demonstrate the proof-of-concept of the approach using measured data.

The solution framework we will use is referred to as Point Source Likelihood (PSL) [15], [29], [30]. PSL requires the knowledge of a detector's position and orientation in 3D as it collects gamma-ray events, as well as knowledge of the detector's angular response. The goal of PSL is to exploit the full 3-D trajectory and orientation of a freely moving detector system, together with its (often sparse) gamma-ray event data, and infer the position and activity of point sources, including uncertainties on all quantities. To achieve this goal, PSL uses a sparse representation of the problem, namely that a single point source and constant background give rise to the detector measurements, and it tests for the possible presence of a point source at a number of fixed positions in space. PSL has also been implemented with a continuous solver instead of using discrete points [15], and it has been extended to successfully solve for multiple point sources [29].

In this paper we will show how PSL can be extended to include the attenuation of material in the scene (Section II) and demonstrate with a toy model that fitting the attenuation parameter can return the correct result (Section II-C). We then apply the method to measurements of sources in experimental scenarios (Section III) and conclude by discussing the effectiveness and limitations of the approach (Section IV).

II. METHODOLOGY

In this section, we will explain the existing PSL algorithm, and then extend and validate a version that includes attenuation in the scene.

A. PSL without attenuation

In the existing PSL approach, the 3-D environment around the detection system is first populated with possible positions of point sources (test points). For example, a regular grid of 3-D space around the detector's path may be used, and that grid may potentially be downselected to consider only those grid points that are near a surface (inferred from, e.g., a point cloud). The photon events in question are assumed to come either from a photopeak or from a background that is constant in time; downscattering is neglected. A response matrix is generated that gives the average number of photopeak photons that would be detected in measurement i for a source of unit activity at test point j. The response matrix $\mathbf{R}$, which relates source activity to detector count rates, is calculated using the formula

$$R_{ij} = \frac{A(\mathbf{q}_i, \hat{\mathbf{r}}_{ij})}{4\pi |\mathbf{r}_{ij}|^2} BC\tau_{ij}, \tag{1}$$

where $\mathbf{q}_i$ is the system's orientation, $\mathbf{r}_{ij}$ is the vector from the system to the test point, $A(\mathbf{q}_i, \hat{\mathbf{r}}_{ij})$ is the effective area (geometric area times efficiency) given the system orientation and direction to the point, which we have assumed is in the far field, B is the branching ratio for the gamma-ray emission of interest, C is a conversion factor to relate the source activity units to the number of nuclear decays per second, and τ_{ij} is the fraction of unattenuated photopeak photons along $\mathbf{r}_{ij}$. For the case of no attenuation, we will assume $\tau_{ij} = 1$.

For each test point j, a linear model is considered that assumes all detections are either from a point source at j or a constant background:

$$n_i \sim \text{Poisson}(\mu_{ij}), \tag{2}$$
$$\mu_{ij} \equiv (R_{ij}s + b)\Delta t_i, \tag{3}$$

where s is the activity of the source at the test point, b is the background count rate, and Δt_i is the integration time. To simplify the description of the linear model, we introduce the system tensor

$$X_{ij0} = R_{ij}\Delta t_i \tag{4}$$
$$X_{ij1} = \Delta t_i \tag{5}$$

and then shift notation by vectorizing over the measurement index i and using boldface for the resulting vectors; e.g., the measured photopeak counts n_i become $\mathbf{n}$, the mean counts μ_{ij} become $\boldsymbol{\mu}_j$, and the jth column of R_{ij} is $\mathbf{R}_j$. In this notation, X is considered to be a set of 2-D system matrices (dimensions are the number of measurements $\times$ 2) for each test point j:

$$\mathbf{X}_j = [\mathbf{R}_j \odot \boldsymbol{\Delta t}, \ \boldsymbol{\Delta t}], \tag{6}$$

where $\odot$ is element-wise multiplication. Grouping s and b into the parameter vector $\boldsymbol{\theta}^\top = [s, \ b]^\top$, the problem solved

at each test point j (equation (2) and equation (3)) can finally be rewritten as the following matrix equation:

$$\mathbf{n} \sim \text{Poisson}(\boldsymbol{\mu}_j = \mathbf{X}_j \boldsymbol{\theta}). \tag{7}$$

In accordance with Equation (7), the optimal value of $\boldsymbol{\theta}$ is found by minimizing the negative Poisson log likelihood function:

$$-\log L_j(\boldsymbol{\theta}) = \sum_i \left[\mu_{ij} - n_i \log \mu_{ij} + \log(n_i!)\right] \tag{8}$$

$$= \sum_i \left[(\mathbf{X}_j \boldsymbol{\theta})_i - n_i \log(\mathbf{X}_j \boldsymbol{\theta})_i + \log(n_i!)\right]. \tag{9}$$

The negative log likelihood function $-\log L_j(\boldsymbol{\theta})$ is convex in $\boldsymbol{\theta}$ [31], which means it has a single, global maximum, and this property can be quickly established by examining its Hessian:

$$\mathbf{H}_j(\boldsymbol{\theta}) = \begin{bmatrix} \sum_i \frac{R_{ij}^2 \Delta t_i^2 n_i}{\mu_{ij}^2} & \sum_i \frac{R_{ij} \Delta t_i^2 n_i}{\mu_{ij}^2} \\ \sum_i \frac{R_{ij} \Delta t_i^2 n_i}{\mu_{ij}^2} & \sum_i \frac{\Delta t_i^2 n_i}{\mu_{ij}^2} \end{bmatrix} \tag{10}$$

$$= \mathbf{X}_j^\top \text{diag}\left(\frac{\mathbf{n}}{(\mathbf{X}_j \boldsymbol{\theta})^2}\right) \mathbf{X}_j. \tag{11}$$

By defining

$$\mathbf{v}_j^s \equiv \frac{\mathbf{R}_j \odot \Delta\mathbf{t} \odot \sqrt{\mathbf{n}}}{\mathbf{X}_j \boldsymbol{\theta}}, \quad \mathbf{v}_j^b \equiv \frac{\Delta\mathbf{t} \odot \sqrt{\mathbf{n}}}{\mathbf{X}_j \boldsymbol{\theta}}, \tag{12}$$

where the square root and division are performed element-wise, we can write the Hessian in the form

$$\mathbf{H}_j = \begin{bmatrix} \mathbf{v}_j^s \cdot \mathbf{v}_j^s & \mathbf{v}_j^s \cdot \mathbf{v}_j^b \\ \mathbf{v}_j^s \cdot \mathbf{v}_j^b & \mathbf{v}_j^b \cdot \mathbf{v}_j^b \end{bmatrix}. \tag{13}$$

And therefore

$$\text{tr}\,\mathbf{H}_j = \|\mathbf{v}_j^s\|^2 + \|\mathbf{v}_j^b\|^2 \geq 0 \tag{14}$$

$$\det \mathbf{H}_j = \|\mathbf{v}_j^s\|^2 \|\mathbf{v}_j^b\|^2 - \left(\mathbf{v}_j^s \cdot \mathbf{v}_j^b\right)^2 \geq 0, \tag{15}$$

where the second inequality follows from the Cauchy-Schwarz inequality. Because $\mathbf{H}_j$ is a symmetric 2×2 matrix and its trace and determinant are both non-negative, it follows that both of its eigenvalues are non-negative, making $\mathbf{H}_j$ positive semi-definite, and thus $-\log L_j$ is everywhere a convex function of $\boldsymbol{\theta}$. Therefore $-\log L_j$ has a single, global maximum at a point that we will denote $\hat{\boldsymbol{\theta}}_j$. (The only possibility of a degenerate solution is if $n_i = 0$ $\forall i$, a case we avoid by the implicit assumption there is at least one measured event.)

To find $\hat{\boldsymbol{\theta}}_j$ for each test point j, the multiplicative Maximum Likelihood Expectation Maximization (MLEM) update rules for Poisson data were used [31]. Starting with any initial non-zero guess for $\hat{\boldsymbol{\theta}}_j$, the multiplicative update rule is

$$\hat{\boldsymbol{\theta}}_j \leftarrow \hat{\boldsymbol{\theta}}_j \odot \left(\frac{\mathbf{X}_j^\top \cdot \frac{\mathbf{n}}{\mathbf{X}_j \hat{\boldsymbol{\theta}}_j}}{\mathbf{X}_j^\top \cdot \mathbf{1}_M}\right), \tag{16}$$

where M is the number of measurements and $\mathbf{1}_M$ is a column vector of M ones. For each test point, at least 100 iterations of the multiplicative update rules were performed, and iterations were terminated once the change in all parameters was less than 10^{-5}. Then the negative log likelihood for each test point

was calculated was calculated at the best fit parameters:

$$-\log \hat{L}_j \equiv -\log L_j(\hat{\boldsymbol{\theta}}_j). \tag{17}$$

The overall most likely location for the point source was determined by finding the minimum negative log likelihood, $-\log \hat{L}_{\text{min}}$, and its corresponding test point j_{min}. We note that although the optimization to find $\hat{\boldsymbol{\theta}}_j$ is convex and therefore a global maximum exists, the optimization over j (i.e., over the three spatial dimensions) is not guaranteed to be convex.

Spatial confidence intervals were determined by using the likelihood ratio test (LRT), where the null hypothesis is the best fit model with all parameters held constant. The LRT statistic $\Lambda_j = 2(-\log \hat{L}_j + \log \hat{L}_{\text{min}})$ is approximately distributed as a chi-squared distribution with five degrees of freedom: one for s, one for b, and three degrees of freedom for the three spatial dimensions, even though they are not explicit model parameters [32]. The necessity of including these three implicit spatial degrees of freedom to correctly estimate confidence intervals was confirmed through simulations. Choosing an α to construct a $1-\alpha$ confidence interval (e.g., $\alpha = 0.05$ for a 95% confidence interval) yields the following LRT threshold:

$$\Lambda_{\text{threshold}}(\alpha) = \Phi_{\chi_5^2}^{-1}(1-\alpha), \tag{18}$$

where $\Phi_{\chi_5^2}^{-1}$ is the inverse cumulative distribution function of the χ^2 distribution with five degrees of freedom. Parametrizing confidence intervals instead using the z-sigma unit normal equivalent yields:

$$\alpha(z) = 2\left(1 - \Phi_{\text{normal}}(z)\right) \tag{19}$$

$$= 1 - \text{erf}\left(\frac{z}{\sqrt{2}}\right) \tag{20}$$

$$\Lambda_{\text{threshold}}(z) = \Phi_{\chi_5^2}^{-1}\left[\text{erf}\left(\frac{z}{\sqrt{2}}\right)\right], \tag{21}$$

where Φ_{normal} is the cumulative distribution function of the unit normal distribution. All of the test points whose Λ_j values are below the chosen threshold are included in the $1-\alpha$ or z-sigma confidence interval.

Source activity confidence intervals were performed in a different manner. The source activity interval could be estimated as the interval that encloses the $\hat{s}_j$ values of all test points within the spatial confidence interval. However, in practice, especially if the number of such points is low, this method might not be conservative enough. To compensate for this problem, a confidence interval for $\hat{s}_j$ was developed for each test point, and the union of these confidence intervals was used as the overall confidence interval for s. To estimate the confidence interval for $\hat{s}_j$ at test point j, the observed Fisher information matrix was used, which is just the Hessian of the negative log likelihood evaluated at $\hat{\boldsymbol{\theta}}_j$:

$$\mathbf{F}_j = \mathbf{X}_j^\top \text{diag}\left(\frac{\mathbf{n}}{(\mathbf{X}_j \hat{\boldsymbol{\theta}}_j)^2}\right) \mathbf{X}_j. \tag{22}$$

Holding the test point position constant but considering hypothetical statistical fluctuations (e.g., performing a parametric bootstrap), the negative log likelihood will vary in the neighborhood of $\hat{\boldsymbol{\theta}}_j$ according to its Taylor expansion (where

the first derivative vanishes by the definition of maximum likelihood):

$$-\log L_j^* \approx -\log \hat{L}_j + \frac{1}{2}(\boldsymbol{\theta}_j^* - \hat{\boldsymbol{\theta}}_j)^\top \mathbf{F}_j(\boldsymbol{\theta}_j^* - \hat{\boldsymbol{\theta}}_j) \quad (23)$$

We then select the range of $\boldsymbol{\theta}_j^*$ values that result in a negative log likelihood below the threshold:

$$\Lambda_j + (\boldsymbol{\theta}_j^* - \hat{\boldsymbol{\theta}}_j)^\top \mathbf{F}_j(\boldsymbol{\theta}_j^* - \hat{\boldsymbol{\theta}}_j) \leq \Lambda_{\text{threshold}}(z). \quad (24)$$

When the above condition reaches equality, an ellipse of $\boldsymbol{\theta}_j^*$ is defined, although it may be clipped at zero in one or both dimensions, a complication that would decrease the effective number of degrees of freedom and which we will ignore for our purposes of estimation here.

We want to find the maximum range of s_j^* (the first dimension of $\boldsymbol{\theta}_j^*$) given $\mathbf{F}_j$, which happens at the critical values of s_j^* given by:

$$s_{j\pm}^{\text{crit}} = \hat{s}_j \pm \sqrt{\frac{(\Lambda_{\text{threshold}} - \Lambda_j)F_{j;11}}{\det \mathbf{F}_j}}, \quad (25)$$

and s_{j-}^{crit} is clipped at zero if negative. Note that $F_{j;11}$ and $\det \mathbf{F}_j$ are both non-negative because of the properties of the Hessian discussed earlier.

The final range of critical values of s_j^* are chosen as the z-sigma confidence interval for $\hat{s}_j$. The overall z-sigma confidence interval of $s_{\min}$ is then estimated by finding the minimum and maximum critical values for all points within the spatial confidence interval; i.e., all test points where $\Lambda_j \leq \Lambda_{\text{threshold}}$.

B. PSL with an attenuation parameter

The basic PSL approach from the previous section was modified to introduce a new parameter — the photon mean free path (MFP) in any material in the scene. The primary change is in the calculation of the response matrix element R_{ij}, where the fraction of unattenuated photopeak photons τ_{ij} is found. To calculate τ_{ij}, the 3-D environment was represented using a regular grid of voxels that are labeled as either occupied or unoccupied according to whether they included any LiDAR points. Restricting the analysis to only photons in the photopeak region, and assuming a single class of solid material, the attenuation model becomes dependent only on the mean free paths of the photons in any intervening material (air or solid):

$$\tau_{ij} = \exp\left(-r_{ij}^{\text{air}}/\lambda_{\text{air}}\right)\exp\left(-r_{ij}^{\text{solid}}/\lambda_{\text{solid}}\right), \quad (26)$$

where r_{ij}^{air} and r_{ij}^{solid} are the total lengths of air and solid material that are traversed by $\mathbf{r}_{ij}$, and λ_{air} and λ_{solid} are the photon mean free paths.

Ray casting was used to calculate the distances traversed through occupied and unoccupied voxels between any two points, and these distances were identified as r_{ij}^{solid} and r_{ij}^{air}, respectively. The engine used to perform the ray casting was written in Python and used the Amanatides and Woo voxel traversal algorithm [33]. The algorithm is described in Algorithm 1 and illustrated in Fig. 1.
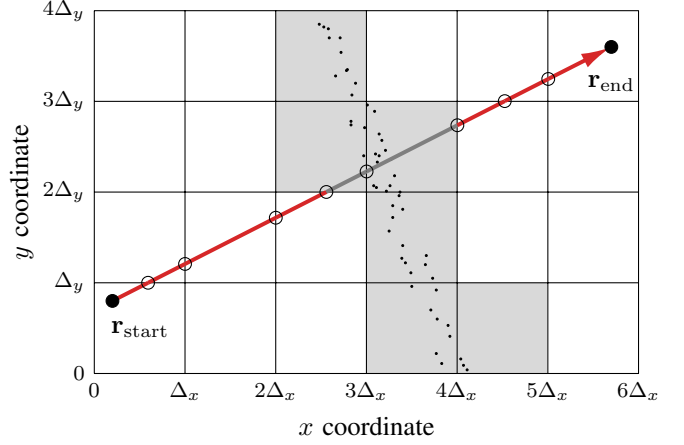

Fig. 1. Schematic of the ray-casting procedure, shown in two dimensions for simplicity. The gridding is indicative of voxel edges. Points within the shaded voxels represent point-cloud returns, thereby causing the respective containing voxels to be considered occupied. The ray-casting algorithm starts at $\mathbf{r}_{\text{start}}$ and visits each intersection point (open circles) until it reaches $\mathbf{r}_{\text{end}}$. The distance traversed through occupied voxels (gray) is tallied separately from the distance traversed through unoccupied voxels (red).

Algorithm 1 Ray-Casting Algorithm (based on [33])

1: **procedure** RAYCAST($\mathbf{r}_{\text{start}}, \mathbf{r}_{\text{end}}, \boldsymbol{\Delta}$)
2: $\quad r^{\text{air}} = 0$
3: $\quad r^{\text{solid}} = 0$
4: $\quad \mathbf{k} = (\mathbf{r}_{\text{end}} - \mathbf{r}_{\text{start}})/\|\mathbf{r}_{\text{end}} - \mathbf{r}_{\text{start}}\|$ $\quad \triangleright$ Calculate direction
5: $\quad \mathbf{r} = \mathbf{r}_{\text{start}}$ $\quad\quad\quad\quad\quad\quad\quad\quad\quad\quad \triangleright$ Start at origin
6: $\quad (i_x, i_y, i_z) = (\lfloor r_x/\Delta_x \rfloor, \lfloor r_y/\Delta_y \rfloor, \lfloor r_z/\Delta_z \rfloor)$ $\triangleright$ Set voxel indices
7: $\quad d_x = 1$ if $k_x > 0$, else 0 $\quad\quad\quad \triangleright$ Set voxel index changes
8: $\quad d_y = 1$ if $k_y > 0$, else 0
9: $\quad d_z = 1$ if $k_z > 0$, else 0
10: $\quad$ **while** $\mathbf{r} \neq \mathbf{r}_{\text{end}}$ **do**
11: $\quad\quad t_x \leftarrow [(i_x + d_x)\Delta_x - r_x]/k_x$ $\triangleright$ Distances to $x/y/z$ boundaries
12: $\quad\quad t_y \leftarrow [(i_y + d_y)\Delta_y - r_y]/k_y$
13: $\quad\quad t_z \leftarrow [(i_z + d_z)\Delta_z - r_z]/k_z$
14: $\quad\quad t_{\text{end}} = \|\mathbf{r} - \mathbf{r}_{\text{end}}\|$ $\quad\quad\quad \triangleright$ Distance to destination
15: $\quad\quad t = \min(t_x, t_y, t_z, t_{\text{end}})$ $\quad \triangleright$ Choose shortest distance
16: $\quad\quad$ **if** occupied(i_x, i_y, i_z) **then** $\quad \triangleright$ Increment traveled distances
17: $\quad\quad\quad r^{\text{solid}} \leftarrow r^{\text{solid}} + t$
18: $\quad\quad$ **else**
19: $\quad\quad\quad r^{\text{air}} \leftarrow r^{\text{air}} + t$
20: $\quad\quad$ **end if**
21: $\quad\quad \mathbf{r} \leftarrow \mathbf{r} + t\mathbf{k}$ $\quad\quad\quad\quad\quad\quad \triangleright$ Move to next point
22: $\quad\quad$ **if** $t = t_x$ **then** $\quad\quad\quad\quad \triangleright$ Update voxel indices
23: $\quad\quad\quad i_x \leftarrow i_x + 2d_x - 1$ unless $k_x = 0$
24: $\quad\quad$ **else if** $t = t_y$ **then**
25: $\quad\quad\quad i_y \leftarrow i_y + 2d_y - 1$ unless $k_y = 0$
26: $\quad\quad$ **else if** $t = t_z$ **then**
27: $\quad\quad\quad i_z \leftarrow i_z + 2d_z - 1$ unless $k_z = 0$
28: $\quad\quad$ **end if**
29: $\quad$ **end while**
30: **end procedure**

With r_{ij}^{solid} calculated, it remains to find the value of λ_{solid}. The value of λ_{air} can be obtained from tables using the photopeak energy and assuming dry air at standard temperature and pressure; $\lambda_{\text{air}} = 107.8$ m and 83.4 m were used for the analysis of 662 keV and 356 keV photopeak events, respectively [34], [35]. The approach taken was to treat λ_{solid} as another parameter of PSL to optimize over, in addition to s, b, and position (x, y, z). In this proof-of-concept, the optimization was done in a brute-force manner — a grid of λ_{solid} values was chosen and PSL was solved over a four-

dimensional grid of $(x, y, z, \lambda_{\text{solid}})$. The test point index j was expanded to denote both spatial position and λ_{solid} value, and then the PSL solution with the smallest $-\log \hat{L}_{\min}$ was chosen as the best overall point-source model. Because we now effectively have six degrees of freedom instead of five, a χ_6^2 distribution was used when calculating the confidence intervals (i.e., using the LRT threshold in Equation (21)). When calculating confidence intervals, all PSL solutions in the four-dimensional space that were below the likelihood threshold were used. Analogous to spatial confidence intervals, a confidence interval for λ_{solid} can likewise be generated.

C. Validation of the approach using a toy model

A toy model was developed to simulate the effect of a point source inside a simple structure with external walls, internal walls, windows, and doors. The building was constructed using a regular 3-D voxel space with a voxel size of 15 cm. It consisted of an 8×8-m external wall that was one voxel thick, with some portions of the wall removed to represent windows and doors. Internal walls were added in the form of one-voxel thick structures. The material making up the building was assumed to have an MFP of 0.30 m for 662 keV photons, which is roughly the value for low density wood. A hypothetical detector with a spherically symmetric response function ($A = 10 \, \text{cm}^2$) was moved along a 10×10-m square surrounding the structure over the course of 60 seconds while traveling at a constant speed, and data were recorded at a rate of 5 Hz. The height of the detector varied as a sinusoid of amplitude 40 cm to simulate the motion of walking and add variation in the vertical dimension. A 500-µCi ^{137}Cs point source was placed inside the structure 1 meter above the floor at the same mean height as the detector. The resulting structure, detector path, and source location is shown in Fig. 2.

PSL was performed with and without fitting the attenuation from the structure, using all voxel centers inside the structure as test points. To optimize over MFP, PSL was solved at 100 values spaced logarithmically from 5 cm to 100 m. The shape of the best fit negative log likelihood as a function of MFP was concave, and thus there was only one local optimum for λ_{solid}, which was also the global optimum, which is 0.37 m. Note, however, that the negative log likelihood function is not in general guaranteed to be concave along this dimension, nor in any of the three spatial dimensions. The algorithm is able to provide a 2σ confidence interval for the mean free path in the same way as it does for the spatial dimensions by noting the range of MFP values for which any test points exist with Λ values below $\Lambda_{\text{threshold}}$; for the toy model, this interval is 0.25–0.58 m. The best fit source activity was 525 µCi, with a 2σ confidence interval of 440–760 µCi, which is in agreement with the simulated activity. In addition, the 2σ spatial confidence interval enclosed the true source position. In contrast, the PSL solution that ignored attenuation from occupied voxels returned a 2σ spatial confidence interval whose nearest boundary was approximately 40 cm from the true position and gave a source activity confidence interval of 270–380 µCi, which excludes the true activity. Fig. 3 shows the simulated count rates and the 2-sigma bounds of the most
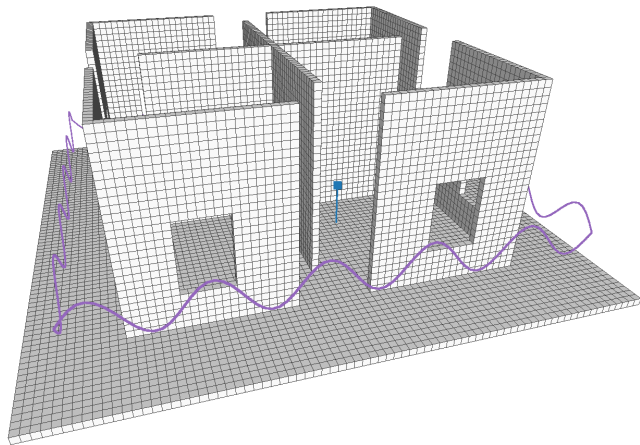

Fig. 2. A three-dimensional rendering of the toy model used, showing the path of the detector (purple) and the position of the source (blue dot, with vertical line to indicate horizontal location).

probable source locations in the point cloud for the best PSL solutions when attenuation is optimized versus set to λ_{air}.

III. RESULTS FOR EXPERIMENTAL DATA

In order to test the approach, experimental data were taken on 17 August 2020 with sources in a realistic scenario. The scenario consisted of several stacked 20-foot shipping containers in a field at the Richmond Field Station (RFS) in Richmond, CA. Two sources were placed in the scene: a ^{137}Cs source with an activity of 1848 µCi was placed on the outside of a container in a narrow gap between the containers, and a 638-µCi ^{133}Ba source placed inside on the floor of an empty container in a second grouping of containers. The sources were approximately 30 m away from each other, and the path of the system allowed two subsets of the data to be chosen that effectively separated the source measurements into two independent measurements.

The data were collected with the MiniPRISM system, which consists of up to 64 coplanar grid CdZnTe detectors, each of which is a $1 \, \text{cm}^3$ cube [36]. MiniPRISM's detectors are arranged into a partially filled 6×6×4 grid of potential detector locations, with the detectors in an optimized arrangement for detection sensitivity and active coded mask imaging performance. The detector system is integrated with a package of contextual sensors, including a LiDAR, Inertial Measurement Unit (IMU), and camera (Fig. 4) and mounted on an small Unmanned Aerial System (sUAS) platform. Although the data are individually read out by detector, for this analysis the detector events were collected together as if the system were a single, monolithic detector to maintain simplicity and keep computation times manageable while demonstrating efficacy in modeling attenuation. A measurement-validated simulated response function in all 4π steradians was used when performing PSL [30], and the simulations used the actual configuration of 58 detectors used in the measurement. Only the responses for the 54 detectors that had adequate performance at the time were summed together and used
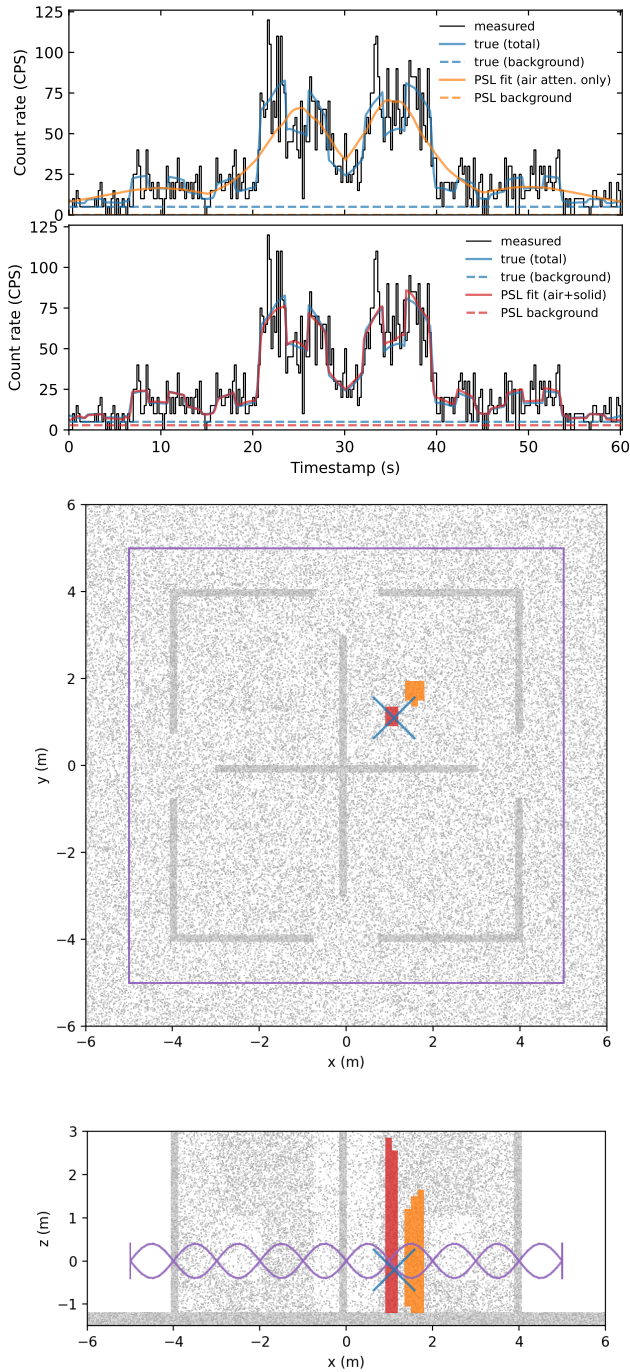
Fig. 3. The simulated counts in the detector for the toy model, showing the best fit when only air attenuation is included (top) and when a solid attenuation parameter is fit (second from top). The resulting spatial confidence intervals are shown in the bottom two figures, where the 2-sigma confidence intervals are shown as red and orange volumes, for the with-solid and air-only attenuation models, respectively. The simulated trajectory of the system is shown in purple and the true source location is shown as a blue cross. The point cloud in these plots is a simulated point cloud based on the occupied voxels of the toy model.

in the analysis. The on-board LiDAR and IMU were used to perform Simultaneous Localization and Mapping (SLAM) using Google Cartographer [37]. SLAM solves for a fixed frame and outputs the path and orientation of the system within
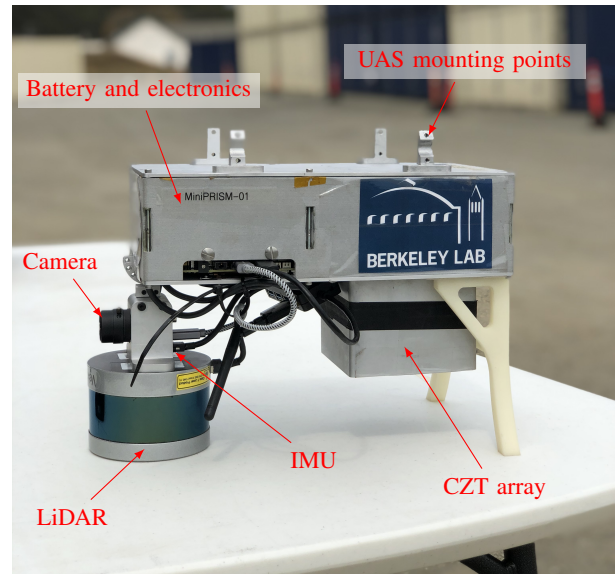

Fig. 4. The MiniPRISM detector system before being mounted on the UAS platform.

that frame, as well as LiDAR points mapped into that frame. SLAM is performed in real-time by the on-board computer, and PSL without attenuation and other data products are served to the user in real-time.

A. Cs-137 in gap between shipping containers

To search for the ^{137}Cs source, the sUAS was flown along both sides of the container stacks at an average standoff of 4 m from the sides of the containers and at an altitude of 3 m above ground level (AGL), and then flown at 8 m AGL over the center of the stacks (and about 3 m above the top of the stack) where the source was located, for a total duration of about 220 s. Data were binned at 5 Hz for analysis, and the spectral region from 620–700 keV was selected to capture the 662 keV photopeak.[1] A voxel grid with 13.5-cm pitch was rotated and translated by hand to align it with the container stack and exploit its rectilinear shape, and any voxels containing points from the LiDAR point cloud were marked as occupied. Those voxels within individual containers were not considered occupied. The resulting occupied voxel model is shown in Fig. 5.

PSL was performed using the centers of all voxels within the grid as test points and optimizing λ_{solid} over 100 values logarithmically spaced from 0.045 m to 107.8 m (λ_{air} for 662 keV). The ray-casting calculation took 60 minutes on a four-core Intel i7 CPU, and each MFP optimization step took 90 s, for a total of 210 minutes for the entire optimization. As in the toy model, the curve of negative log likelihood versus MFP was found to be concave (the blue line in Fig. 6). The optimal MFP obtained was 0.82 m, with a 2σ confidence interval of 0.60–1.32 m. The most likely source activity was

---

[1] Although the detectors are CdZnTe and can in principle achieve an energy resolution of 2% FWHM [38], the individual channel nonlinearities and gain drift were difficult to correct to the level of the ideal resolution. In addition, any non-photopeak events can be fit as background by PSL.
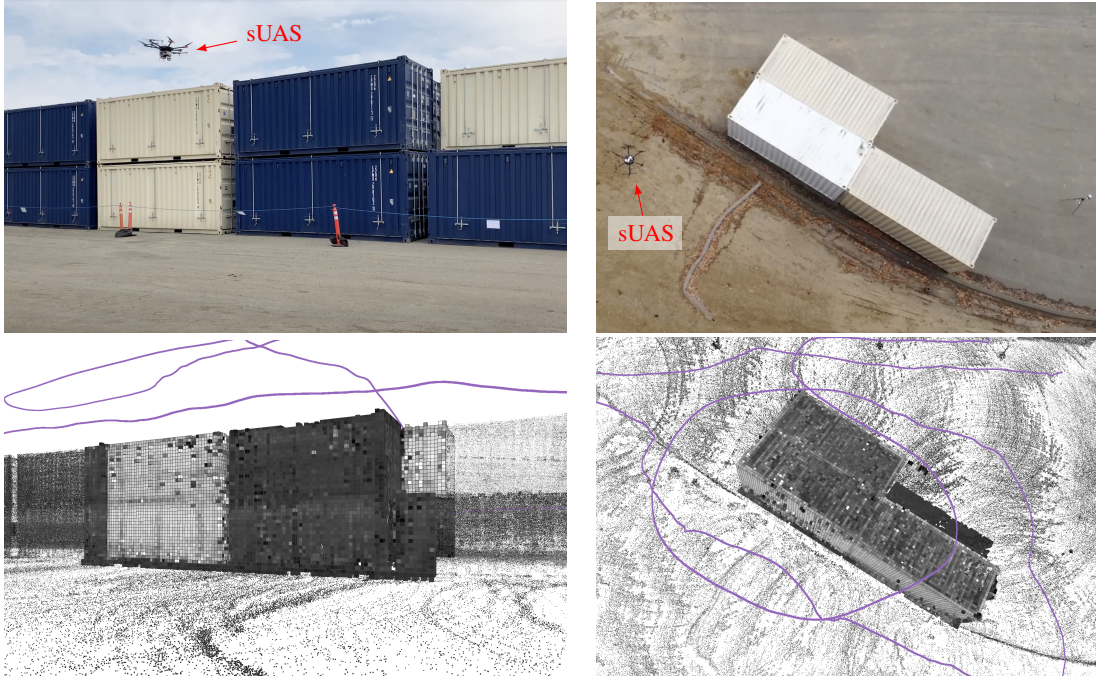
Fig. 5. The occupied voxel models made from the LiDAR point clouds. The ^{137}Cs source scenario (top left), voxelized at 13.5 cm resolution (bottom left). The ^{133}Ba source scenario (top right), voxelized at 12 cm resolution (bottom right). The purple path is the path of the detector system, and the grayscale points are the LiDAR point cloud colorized by near-infrared reflectivity. In both of the top images, the sUAS carrying MiniPRISM is indicated.
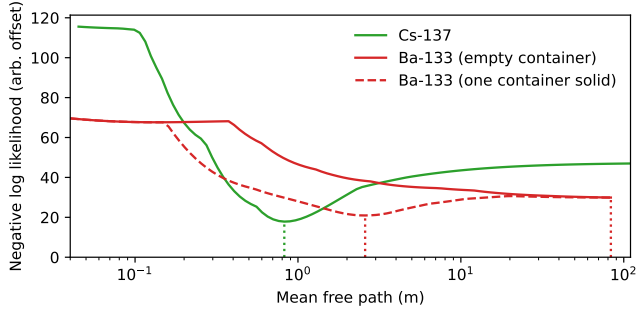

Fig. 6. The best negative log likelihood values as a function of λ_{solid} for the experimental data.

1440 μCi, with a 2σ confidence interval of 960–2070 μCi, which includes the true activity at the time the measurement was made (1848 μCi). Without attenuation from occupied voxels, the confidence interval is 380–730 μCi, which excludes the true activity. The 2σ spatial confidence interval was limited to only five 13.5 cm voxels, all falling inside the gap between containers where the source was actually located. The source ground truth position fell just outside of these five voxels by about 10 cm, which is on the order of the voxelization and fidelity of the ground truth itself. These results are shown in Fig. 7.

The best fit value of λ_{solid} seems at first to be far too large — the containers are made of steel, so naïvely the MFP should be approximately the tabulated value 0.0176 m for 662 keV [34], [35]. This apparent discrepancy will be addressed in Section IV.

B. Ba-133 in an empty container

For the ^{133}Ba source, since the second stack was only a single layer of three containers, the UAS flew around the stack once at approximately 2 m above ground level and roughly 3 m standoff from the sides of the containers, and a second time at 5 m AGL, which was 2 m above the top of the containers, for a total duration of about 145 s. This grouping of containers consisted of three containers only in a single layer (Fig. 5). Data were binned at 5 Hz for analysis, and the spectral region from 315–385 keV was selected to capture the 356 keV photopeak. Because the spatial region of interest was smaller than in the ^{137}Cs case, a finer voxel pitch of 12 cm was possible. Once again the voxel grid was aligned to the containers to exploit their rectangular shape.

For PSL, λ_{solid} was swept over 100 values logarithmically spaced from 0.04 m to λ_{air}=83.4 m. The ray-casting calculation took 30 minutes on the same system as the ^{137}Cs analysis, and each MFP optimization step took 40 seconds, for a total of 100 minutes for the entire optimization. Unlike the toy model and the ^{137}Cs data, the curve of negative log likelihood versus MFP was not concave. In addition, the negative log likelihood generally decreased with increasing MFP, leading to an optimal MFP of 83.4 m, or essentially no attenuation from occupied voxels.

Inquiring further, it was discovered that the container adjacent to the empty container with the source was filled with various pieces of large scientific equipment, including many items made of steel. So the same analysis was performed but marking all voxels inside that one container as occupied. Once this was done, the log likelihood-MFP curve became nearly completely concave again, and the optimal MFP was found
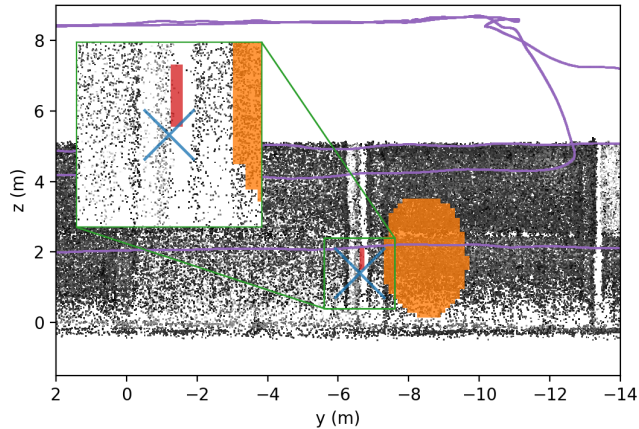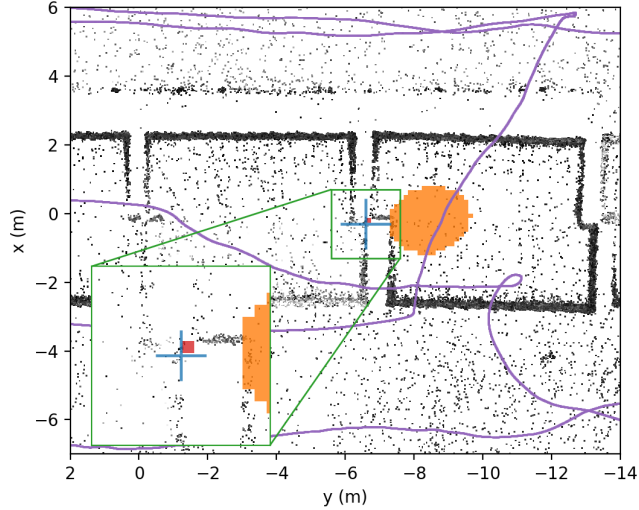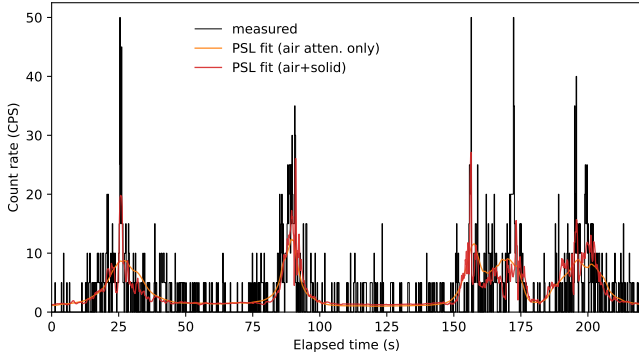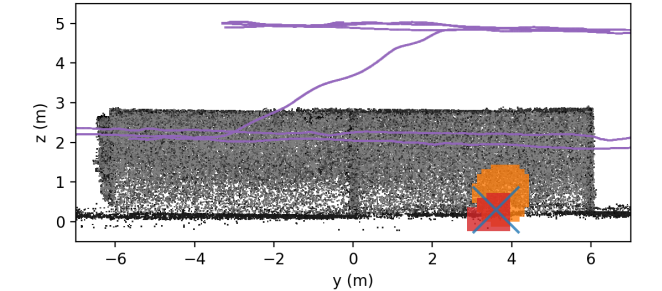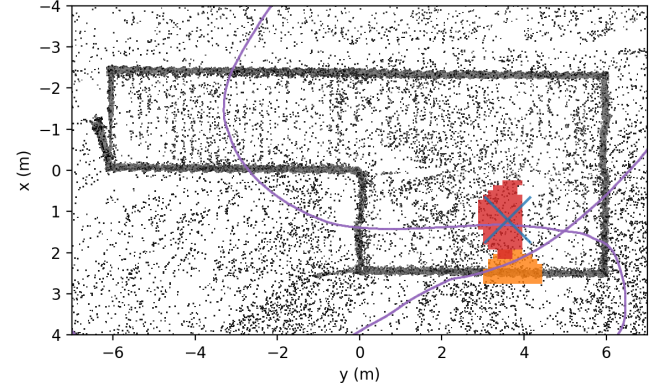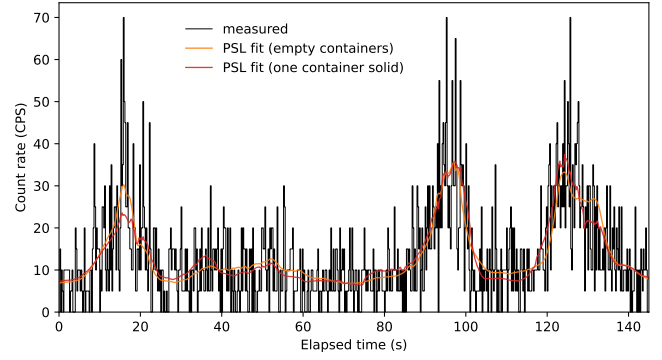
Fig. 8. Results for ^{133}Ba showing the best fit model when the containers are assumed to be empty (orange) and when all voxels inside the top right container are marked as occupied (red). The top plot shows the count rates, while the bottom two plots show the 2σ spatial confidence intervals for top-down and side views in the same colors as the count rate plot. The ground truth is once again shown with a blue cross. In this case, the result assuming the containers are empty coincidences with the result when solid attenuation is ignored, so that model and confidence intervals are not shown.

Fig. 7. Results for ^{137}Cs showing the best fit model when no attenuation is assumed for occupied voxels (orange) and when the optimal MFP is found for occupied voxels (red). The top plot shows the count rates, while the bottom two plots show the 2σ spatial confidence intervals for top-down and side views in the same colors as the count rate plot. The ground truth is shown with a blue cross. Insets are given to zoom in on the 2×2 m region around the ground truth. Note that the red region is small, taking up only five voxels, and localizes the source to within the gap between the containers.

to be 2.58 m with a 2σ confidence interval of 1.11–7.05 m (see Fig. 6). Moreover, the 2σ confidence interval for the source activity shifted from 280–550 to 425–800 µCi, which now includes the true activity (638 µCi). At the same time, the 2σ spatial confidence interval changes from excluding to

including the ground truth (Fig. 8).

As with the ^{137}Cs analysis, the best fit value of λ_{solid} again is much larger than the tabulated value of 0.0133 m for 356 keV photons in steel [34], [35], and this will be discussed in the next section.

IV. DISCUSSION

We have shown that attenuation by objects in the environment can be a major influence on the effectiveness of certain point source reconstructions, and it is possible to use three-dimensional information to estimate the effect of attenuation by material in the environment and obtain the correct location and activity of a point source, at least under certain conditions.

To demonstrate this result, experimental data were collected for two sources in shipping containers, and analysis yielded source parameters in agreement with the ground truth.

As noted earlier, the values of the best fit photon MFPs seem at first to be far too large when compared with tabulated values for attenuation by the steel walls of the containers — 2.58 and 0.82 m, versus 0.0133 and 0.0176 m for ^{133}Ba and ^{137}Cs, respectively. For ^{137}Cs, this apparent discrepancy can be reconciled by the fact that the voxels were much thicker than the walls of the containers, which are approximately 2 mm thick, although the corrugation of the steel increases the effective wall thickness to approximately 3 mm [39]. In this case, the relevant parameter is not λ_{solid} but the dimensionless quantity $\lambda_{\text{solid}}/\Delta$, the ratio of the MFP to the voxel pitch, which should be approximately equal to the true MFP (λ_{true}) over the true characteristic wall thickness Δ_{true}. The expected ratio for 662 keV photons is therefore 5.9, in agreement with the 2σ confidence interval 4.5–9.8. Therefore, this scenario is believed to be explained primarily by steel attenuation.

On the other hand, the 2σ confidence interval of the ^{133}Ba ratio $\lambda_{\text{solid}}/\Delta$ is 9.2–58.7, which excludes the tabulated value of 4.4 for the steel walls, but the analysis has already shown that there was attenuation from other materials in addition to the steel walls. Also, the comparison of $\lambda_{\text{solid}}/\Delta$ to $\lambda_{\text{true}}/\Delta_{\text{true}}$ is only valid when the attenuating material is thinner than the voxel size: $\Delta_{\text{true}} < \Delta$. If the attenuating material is thicker than the voxel size, which is the case here for the bulk material inside the container, then the optimal MFP will increase to account for the thicker material: $\lambda_{\text{solid}}/\Delta \sim n_{\text{voxels}} \cdot \lambda_{\text{true}}/\Delta_{\text{true}}$, where $n_{\text{voxels}} \sim \Delta_{\text{true}}/\Delta$ is the number of voxels that the attenuating material spans on average. For this particular measurement, the material does not uniformly fill the container and is of mixed contents, so no simple theoretical comparison can be made.

The analysis of measured data shows that PSL with attenuation estimation can work in at least some real-world scenarios, but it highlights at least one major challenge — by relying on the LiDAR point cloud alone to sense the 3-D environment, the 3-D model is only capable representing surfaces, whereas the contents of the volumes contained within the exterior surfaces are unknown. For some volumes, such as buildings with windows, the LiDAR is able to sense some of the interior and detect interior walls, but for many surfaces such sensing is impossible with LiDAR. When attenuation from surfaces alone can explain most of the modulation of the source signal, then this method works well. This situation was seen in the case where ^{137}Cs was located in the gap between containers. On the other hand, if attenuation cannot be explained by surfaces alone but by the material behind the surfaces, the method will not work as well until other assumptions are included, such as the ^{133}Ba example.

In future work, it will be important to make inferences about the effect of unobserved volumes. One approach could be to draw rays from the LiDAR during the measurement to determine which voxels in the model have not been visible to the LiDAR and thus are indeterminate, i.e., not known to be occupied or unoccupied. PSL can then be performed by making some set of assumptions about the indeterminate voxels, such as introducing a second mean free path parameter and optimizing over it. This approach would add yet another parameter to optimize over, with increased computational burden.

Additional contextual data may be helpful for this problem as well. Visual cameras, combined with modern computer vision techniques, could label materials in the scene or provide some inference about the makeup of objects. For example, knowing that a planar surface is a brick wall could allow one to make an assumption about its attenuation that will be robust for many photon energies without making any direct measurements of the wall's thickness. Another example would be an algorithm identifying cargo containers in the scene, thus allowing an algorithm to posit guesses about what the volume's properties would be if it were empty or filled and to test those different possibilities. A final example could take advantage of automated segmentation of 3-D volumes and a user interface that allows an operator to enter information based on domain knowledge.

Regarding fieldability, the implementation of PSL with attenuation estimation shown in this work does not run in real-time, and far from it (210 minutes for the ^{137}Cs analysis and 100 minutes for the ^{133}Ba analysis). However, the processing here has been done on a single CPU, which is the worst case scenario. In principle, the ray casting can be parallelized and run on GPUs, and a single PSL optimization has already been implemented on a GPU [30]. A better optimization procedure than a brute force grid search and better initial guesses based on contextual information should also be able to speed up evaluation time, and constraints from computer vision classification or operator input could further reduce the computational complexity and afford nearly real-time inference.

V. Acknowledgments

References

[1] R. Kouzes, "Detecting Illicit Nuclear Materials," *American Scientist*, vol. 93, no. 5, p. 422, 2005. [Online]. Available: http://www.americanscientist.org/issues/page2/detecting-illicit-nuclear-materials

[2] R. C. Runkle, L. E. Smith, and A. J. Peurrung, "The photon haystack and emerging radiation detection technology," *Journal of Applied Physics*, vol. 106, no. 4, p. 041101, Aug. 2009. [Online]. Available: https://aip.scitation.org/doi/full/10.1063/1.3207769

[3] V. Dicken, "A new approach towards simultaneous activity and attenuation reconstruction in emission tomography," *Inverse Problems*, vol. 15, no. 4, pp. 931–960, Aug. 1999, publisher: IOP Publishing. [Online]. Available: https://doi.org/10.1088/0266-5611/15/4/307

[4] J. Nuyts, P. Dupont, S. Stroobants, R. Benninck, L. Mortelmans, and P. Suetens, "Simultaneous maximum a posteriori reconstruction of attenuation and activity distributions from emission sinograms," *IEEE Transactions on Medical Imaging*, vol. 18, no. 5, pp. 393–403, May 1999.

[5] D. Gourion, D. Noll, P. Gantet, A. Celler, and J. P. Esquerre, "Attenuation correction using SPECT emission data only," *IEEE Transactions on Nuclear Science*, vol. 49, no. 5, pp. 2172–2179, Oct. 2002.

[6] P. E. Kinahan, B. H. Hasegawa, and T. Beyer, "X-ray-based attenuation correction for positron emission tomography/computed tomography scanners," *Seminars in Nuclear Medicine*, vol. 33, no. 3, pp. 166–179, Jul. 2003. [Online]. Available: https://www.sciencedirect.com/science/article/pii/S0001299803700038

[7] Y. Berker and Y. Li, "Attenuation correction in emission tomography using the emission data—A review," *Medical Physics*, vol. 43, no. 2, pp. 807–832, 2016. [Online]. Available: https://aapm.onlinelibrary.wiley.com/doi/abs/10.1118/1.4938264

[8] R. Backholm, T. A. Bubba, C. Bélanger-Champagne, T. Helin, P. Dendooven, and S. Siltanen, "Simultaneous reconstruction of emission and attenuation in passive gamma emission tomography of spent nuclear fuel," *Inverse problems and imaging*, vol. 14, no. 2, pp. 317–337, Apr. 2020, publisher: American Institute of Mathematical Sciences. [Online]. Available: https://researchportal.helsinki.fi/en/publications/simultaneous-reconstruction-of-emission-and-attenuation-in-passiv

[9] A. Salomon, A. Goedicke, B. Schweizer, T. Aach, and V. Schulz, "Simultaneous Reconstruction of Activity and Attenuation for PET/MR," *IEEE Transactions on Medical Imaging*, vol. 30, no. 3, pp. 804–813, Mar. 2011.

[10] M. Morelande, B. Ristic, and A. Gunatilaka, "Detection and parameter estimation of multiple radioactive sources," in *2007 10th International Conference on Information Fusion*, Jul. 2007, pp. 1–7.

[11] R. Vilim, R. Klann, and J. Thomas, "Integrated Treatment of Detector Arrays for Source Tracking," *Nuclear Technology*, vol. 175, no. 1, pp. 314–325, Jul. 2011. [Online]. Available: https://doi.org/10.13182/NT11-A12303

[12] H. Wan, T. Zhang, and Y. Zhu, "Detection and localization of hidden radioactive sources with spatial statistical method," *Annals of Operations Research*, vol. 192, no. 1, pp. 87–104, Jan. 2012. [Online]. Available: https://doi.org/10.1007/s10479-010-0805-z

[13] B. Deb, "Iterative Estimation of Location and Trajectory of Radioactive Sources With a Networked System of Detectors," *IEEE Transactions on Nuclear Science*, vol. 60, no. 2, pp. 1315–1326, Apr. 2013.

[14] E.-w. Bai, A. Heifetz, P. Raptis, S. Dasgupta, and R. Mudumbai, "Maximum Likelihood Localization of Radioactive Sources Against a Highly Fluctuating Background," *IEEE Transactions on Nuclear Science*, vol. 62, no. 6, pp. 3274–3282, Dec. 2015.

[15] D. Hellfeld, T. H. Y. Joshi, M. S. Bandstra, R. J. Cooper, B. J. Quiter, and K. Vetter, "Gamma-Ray Point-Source Localization and Sparse Image Reconstruction Using Poisson Likelihood," *IEEE Transactions on Nuclear Science*, vol. 66, no. 9, pp. 2088–2099, Sep. 2019.

[16] J. Towler, B. Krawiec, and K. Kochersberger, "Radiation Mapping in Post-Disaster Environments Using an Autonomous Helicopter," *Remote Sensing*, vol. 4, no. 7, pp. 1995–2015, Jul. 2012, number: 7 Publisher: Molecular Diversity Preservation International. [Online]. Available: https://www.mdpi.com/2072-4292/4/7/1995

[17] E. A. Miller, S. M. Robinson, K. K. Anderson, J. D. McCall, A. M. Prinke, J. B. Webster, and C. E. Seifert, "Adaptively Reevaluated Bayesian Localization (ARBL): A novel technique for radiological source localization," *Nuclear Instruments and Methods in Physics Research Section A: Accelerators, Spectrometers, Detectors and Associated Equipment*, vol. 784, pp. 332–338, Jun. 2015. [Online]. Available: http://www.sciencedirect.com/science/article/pii/S0168900215000698

[18] J. Hite, J. Mattingly, D. Archer, M. Willis, A. Rowe, K. Bray, J. Carter, and J. Ghawaly, "Localization of a radioactive source in an urban environment using Bayesian Metropolis methods," *Nuclear Instruments and Methods in Physics Research Section A: Accelerators, Spectrometers, Detectors and Associated Equipment*, vol. 915, pp. 82–93, Jan. 2019. [Online]. Available: https://www.sciencedirect.com/science/article/pii/S016890021831177X

[19] R. B. Anderson, M. Pryor, A. Abeyta, and S. Landsberger, "Mobile Robotic Radiation Surveying With Recursive Bayesian Estimation and Attenuation Modeling," *IEEE Transactions on Automation Science and Engineering*, pp. 1–15, 2020.

[20] J.-C. Chin, N. S. V. Rao, D. K. Y. Yau, M. Shankar, Y. Yang, J. C. Hou, S. Srivathsan, and S. Iyengar, "Identification of low-level point radioactive sources using a sensor network," *ACM Transactions on Sensor Networks*, vol. 7, no. 3, pp. 21:1–21:35, Oct. 2010. [Online]. Available: https://doi.org/10.1145/1807048.1807050

[21] X. Xu, N. S. V. Rao, and S. Sahni, "A computational geometry method for localization using differences of distances," *ACM Transactions on Sensor Networks*, vol. 6, no. 2, pp. 10:1–10:25, Mar. 2010. [Online]. Available: https://doi.org/10.1145/1689239.1689240

[22] N. S. V. Rao, S. Sen, N. J. Prins, D. A. Cooper, R. J. Ledoux, J. B. Costales, K. Kamieniecki, S. E. Korbly, J. K. Thompson, J. Batcheler, R. R. Brooks, and C. Q. Wu, "Network algorithms for detection of radiation sources," *Nuclear Instruments and Methods in Physics Research Section A: Accelerators, Spectrometers, Detectors and Associated Equipment*, vol. 784, pp. 326–331, Jun. 2015.

[Online]. Available: https://www.sciencedirect.com/science/article/pii/S0168900215000686

[23] C. Q. Wu, M. L. Berry, K. M. Grieme, S. Sen, N. S. Rao, R. R. Brooks, and G. Cordone, "Network Detection of Radiation Sources Using Localization-Based Approaches," *IEEE Transactions on Industrial Informatics*, vol. 15, no. 4, pp. 2308–2320, Apr. 2019, conference Name: IEEE Transactions on Industrial Informatics.

[24] R. Vilim and R. Klann, "RadTrac: A System for Detecting, Localizing, and Tracking Radioactive Sources in Real Time," *Nuclear Technology*, vol. 168, no. 1, pp. 61–73, Oct. 2009. [Online]. Available: https://doi.org/10.13182/NT168-61

[25] R. T. Klann, S. C. De la Barrera, and R. B. Vilim, "Treatment of Shielding in Real-Time Source Tracking Software," *Nuclear Technology*, vol. 175, no. 1, pp. 301–313, Jul. 2011. [Online]. Available: https://doi.org/10.13182/NT11-A12302

[26] G. Cordone, R. R. Brooks, S. Sen, N. S. V. Rao, C. Q. Wu, M. L. Berry, and K. M. Grieme, "Improved multi-resolution method for MLE-based localization of radiation sources," in *2017 20th International Conference on Information Fusion (Fusion)*, Jul. 2017, pp. 1–8.

[27] M. K. Sharma, A. B. Alajo, and H. K. Lee, "Three-dimensional localization of low activity gamma-ray sources in real-time scenarios," *Nuclear Instruments and Methods in Physics Research Section A: Accelerators, Spectrometers, Detectors and Associated Equipment*, vol. 813, no. Supplement C, pp. 132–138, Mar. 2016. [Online]. Available: http://www.sciencedirect.com/science/article/pii/S0168900216000036

[28] U. Bhattacharyya and C. Baum, "Estimating the location of a nuclear source in a three-dimensional environment using a two-stage adaptive algorithm," in *2018 IEEE 8th Annual Computing and Communication Workshop and Conference (CCWC)*, Jan. 2018, pp. 8–14.

[29] J. R. Vavrek, D. Hellfeld, M. S. Bandstra, V. Negut, K. Meehan, W. J. Vanderlip, J. W. Cates, R. Pavlovsky, B. J. Quiter, R. J. Cooper, and T. H. Y. Joshi, "Reconstructing the Position and Intensity of Multiple Gamma-Ray Point Sources With a Sparse Parametric Algorithm," *IEEE Transactions on Nuclear Science*, vol. 67, no. 11, pp. 2421–2430, Nov. 2020.

[30] D. Hellfeld, M. S. Bandstra, J. R. Vavrek, D. L. Gunter, J. C. Curtis, M. Salathe, R. Pavlovsky, V. Negut, P. J. Barton, J. W. Cates, B. J. Quiter, R. J. Cooper, K. Vetter, and T. H. Y. Joshi, "Free-moving Quantitative Gamma-ray Imaging," *arXiv:2107.04080 [physics]*, 2021, submitted to Scientific Reports - Nature. [Online]. Available: http://arxiv.org/abs/2107.04080

[31] L. A. Shepp and Y. Vardi, "Maximum Likelihood Reconstruction for Emission Tomography," *IEEE Transactions on Medical Imaging*, vol. 1, no. 2, pp. 113–122, Oct. 1982.

[32] S. S. Wilks, "The Large-Sample Distribution of the Likelihood Ratio for Testing Composite Hypotheses," *The Annals of Mathematical Statistics*, vol. 9, no. 1, pp. 60–62, 1938. [Online]. Available: http://www.jstor.org/stable/2957648

[33] J. Amanatides and A. Woo, "A Fast Voxel Traversal Algorithm for Ray Tracing," *EG 1987-Technical Papers*, 1987. [Online]. Available: https://diglib.eg.org:443/xmlui/handle/10.2312/egtp19871000

[34] R. McConn Jr, C. Gesh, R. Pagh, R. Rucker, and R. Williams III, "Compendium of Material Composition Data for Radiation Transport Modeling," Pacific Northwest National Laboratory, Tech. Rep. PIET-43741-TM-963, PNNL-15870 Rev. 1, 2011. [Online]. Available: https://www.pnnl.gov/main/publications/external/technical_reports/PNNL-15870Rev1.pdf

[35] M. Berger, J. Hubbell, S. Seltzer, J. Chang, J. Coursey, R. Sukumar, D. Zucker, and K. Olsen, "XCOM: Photon Cross Sections Database," NIST Standard Reference Database 8, Tech. Rep., 2010.

[36] R. T. Pavlovsky, J. W. Cates, M. Turqueti, D. Hellfeld, V. Negut, A. Moran, P. J. Barton, K. Vetter, and B. J. Quiter, "MiniPRISM: 3D Realtime Gamma-ray Mapping from Small Unmanned Aerial Systems and Handheld Scenarios," in *2019 IEEE Nuclear Science Symposium and Medical Imaging Conference (NSS/MIC)*, Manchester, UK, 2019.

[37] W. Hess, D. Kohler, H. Rapp, and D. Andor, "Real-Time Loop Closure in 2D LIDAR SLAM," in *2016 IEEE International Conference on Robotics and Automation (ICRA)*, 2016, pp. 1271–1278.

[38] P. N. Luke, M. Amman, and J. S. Lee, "Factors affecting energy resolution of coplanar-grid CdZnTe detectors," *IEEE Transactions on Nuclear Science*, vol. 51, no. 3, pp. 1199–1203, Jun. 2004.

[39] P. C. H. Ling, C. S. Tan, Y. H. Lee, and S. Mohammad, "Technical Information on ISO Shipping Container," *IOP Conference Series: Materials Science and Engineering*, vol. 884, p. 012042, Jul. 2020, publisher: IOP Publishing. [Online]. Available: https://doi.org/10.1088/1757-899x/884/1/012042